

# Influence of Conductive Additives and Binder on the Impedance of Lithium-Ion Battery Electrodes: Effect of an Inhomogeneous Distribution

Mrudula Prasad<sup>a,b</sup>, Simon Hein<sup>a,b</sup>, Timo Danner<sup>a,b,\*</sup>, Benedikt Priffling<sup>c</sup>, Rares Scurtu<sup>d</sup>, Alice Hoffmann<sup>d</sup>, André Hilger<sup>e</sup>, Markus Osenberg<sup>e</sup>, Ingo Manke<sup>e</sup>, Margret Wohlfahrt-Mehrens<sup>d</sup>, Volker Schmidt<sup>c</sup>, Arnulf Latz<sup>a,b,f</sup>

<sup>a</sup>*German Aerospace Center (DLR), Institute of Engineering Thermodynamics, Pfaffenwaldring 38-40, 70569 Stuttgart, Germany*

<sup>b</sup>*Helmholtz-Institut Ulm für Elektrochemische Energiespeicherung (HIU), Helmholtzstraße 11, 89081 Ulm, Germany*

<sup>c</sup>*Ulm University (UUlm), Institute of Stochastics, Helmholtzstraße 18, 89081 Ulm, Germany*

<sup>d</sup>*ZSW-Zentrum für Sonnenenergie- und Wasserstoff-Forschung Baden-Württemberg, Helmholtzstraße 8, 89081 Ulm, Germany*

<sup>e</sup>*Helmholtz-Zentrum Berlin für Materialien und Energie, Hahn-Meitner-Platz 1, 14109 Berlin, Germany*

<sup>f</sup>*Ulm University (UUlm), Institute of Electrochemistry, Albert-Einstein-Allee 47, 89081 Ulm, Germany*

---

## Abstract

The conductive additive and binder domain (CBD) is an essential component of lithium-ion battery electrodes. It enhances the electrical connectivity and mechanical stability within the solid electrode matrix. Migration of the binder during electrode drying can lead to an inhomogeneous distribution of the CBD, impeding transport of lithium ions into the electrodes, and diminishing the electronic pathways between solid particles and the current collector. This is especially prominent in thick electrodes at high drying rates. Therefore, we investigate the effect of a non-uniform CBD distribution on the electrochemical performance of NMC622 electrodes via microstructure-resolved three-dimensional (3D) simulations on virtual electrodes, based on

---

\*Corresponding author:

*Email address:* [timo.danner@dlr.de](mailto:timo.danner@dlr.de) (Timo Danner)

*URL:* <http://www.dlr.de/tt/en/> (Timo Danner)

tomographic image data, and compare them with experimental results. The valuable information derived by combining microstructure-resolved models with electrochemical impedance spectroscopy measurements on symmetric cells under blocking electrolyte conditions is used to characterize the lithium-ion transport in the electrode pore space, including the contributions of the CBD. The effect of this inhomogeneity on electrode performance is then gauged via galvanostatic discharge simulations under changing discharge currents and for varying electrode densities. Through our work, we demonstrate the significance of the CBD distribution and enable predictive simulations for future battery design.

---

## 1. Introduction

Lithium-ion batteries are the dominant power source for mobile applications ranging from portable electronic devices to electric vehicles. Especially in the automotive sector, the demand for improved batteries with high energy density and reduced cost is increasing tremendously. Advances in these two properties are generally seen as a prerequisite to promote the breakthrough of battery electric vehicles. One route towards these targets is the development of cells consisting of electrodes with high areal loading [1–4]. This concept allows to save on passive materials and additionally, has the potential to save processing time during cell assembly. The passive materials in a lithium-ion battery cathode are the conductive carbon, assisting in improving the electronic conductivity of the electrode owing to the low electronic conductivity of the active material (AM) [5], and the polymeric binder, which forms a cohesive web encompassing the cathode materials and adheres them to the current collector (CC) [6, 7]. The carbon black and polymeric binder is assumed to form a composite homogeneous phase with an inherent nanoporosity, referred to as the carbon-binder domain (CBD). This is further encouraged by the high-surface area of the carbon black. However, an intrinsic issue of an electrode with high areal loading is longer transport pathways in the electrode and electrolyte, which reduce the power density of the cells. The presence of CBD results in short-chain intra-CBD, and long-chain AM-CBD electronic conduction networks, as well as tortuous ion transport pathways [8]. At high currents mostly transport limitations in the electrolyte become prominent and reduce the performance of the cell [9, 10]. Several concepts are suggested in the literature in order to improve the transport in the electrolyte [7, 11]. Additionally, due to the high areal loading,

27 new challenges arise in the processing of the electrodes, such as during the  
28 mixing, drying and calendaring steps. Especially for thick electrodes it has  
29 been shown that an unfavourable CBD structure, resulting from features of  
30 the mixing process, decisively impairs their industrially required roll-to-roll  
31 processability [12–15]. A production step that plays a critical role on the final  
32 electrode backbone structure is, the drying process. Nikpour *et al.* adeptly  
33 summarise prior literature on electrode drying, and show experimentally the  
34 evolution of the electrode microstructure during this process [16]. Hence,  
35 when high drying rates are applied, this composite phase migrates conjointly  
36 towards the surface of the electrode due to drag of the evaporating solvent,  
37 and the resulting capillary forces [16–18]. This phenomenon causes an inho-  
38 mogeneous distribution of the CBD from current collector to separator; an  
39 effect that is exacerbated in thicker electrodes. As an outcome of this pro-  
40 cess, the electrodes experience: i) a depletion of CBD at the current collector  
41 deteriorating electronic pathways and the adhesion of the electrode layer, and  
42 ii) accumulation of the CBD at the electrode surface blocking pathways for  
43 electrolyte transport [7]. Both effects have a negative effect on the perfor-  
44 mance of the electrode. The drying time-scale considered is much shorter  
45 than the redistribution time of the AM, hence the convective flow does not  
46 effect the AM backbone structure.

47

48 Several articles [19–30] demonstrate that electrochemical impedance spec-  
49 troscopy (EIS) measurements on symmetrical cells are a very useful tool for  
50 the characterization of lithium-ion transport in the electrode pore space.  
51 Similar EIS measurements in the same setup as in this study have been re-  
52 ported for thinner electrodes. Under ideal conditions (uniform electronic and  
53 ionic conductivities across the electrode), a linear increase of the imaginary  
54 part in a 45 degree angle to the real axis [31, 32] is expected. However, for  
55 thicker electrodes, the presence of a high-frequency semi-circle for experi-  
56 ments conducted under blocking electrolyte conditions [27, 33] was noted.  
57 These semi-circles were witnessed at frequencies higher than the charge-  
58 transfer resistance. Amongst some of the origins for this, the following have  
59 been highlighted in the literature: (i) the contact resistance between the  
60 electrode material and the CC metal [34], (ii) heterogeneity within the meso-  
61 and microporous space of an electrode [35], and (iii) inhomogeneities in the  
62 macroscale distribution of the passive and active materials [27]. These origins  
63 coincide with the effects of applying a high drying rate [17]. In the litera-  
64 ture, there are reports that focus on the influence of the CBD and its volume

65 fraction on battery operation [5, 36–42], on the formation of the conductive  
66 networks [43, 19], and on the effective properties of the CBD itself [44–47].  
67 In most studies, a combination of imaging techniques and electrochemical  
68 characterization is used to evaluate the distribution of active particles, and a  
69 resistor network is used to model the electrochemistry. Zielke *et al.* use trans-  
70 port simulations on a combination of electrodes reconstructed from focused  
71 ion beam scanning electron microscopy (FIB-SEM) tomography and virtu-  
72 ally generated electrodes in order to enrich the information content of the  
73 experimental studies [48]. A similar approach is also described in [37]. In the  
74 majority of the studies, the focus lies on the distribution of the CBD in the  
75 bulk of the electrodes [33], with a focus on the anode side [41, 49]. An analysis  
76 of the effect of an inhomogeneous distribution across the electrode thickness  
77 using symmetrical impedance spectroscopy is provided in [27]. However, a  
78 study which includes physics-informed microstructure-resolved electrochemi-  
79 cal simulations in order to provide a more quantitative analysis of the effect on  
80 the cathode side could not be found in the literature. Hence, in this work, we  
81 attempt to deconvolute the rationality for this unanticipated high-frequency  
82 slope by conducting physics-based microstructure-resolved 3D simulations  
83 and validating them against experiments. Our model inherently considers  
84 the local inhomogeneities in the electrode, as well as the morphology and  
85 distribution of the electrode materials [50–53]. This allows the transport pro-  
86 cesses of the electrolyte within the AM and CBD to be resolved, depending  
87 on the local lithium-ion concentration. We could demonstrate that symmet-  
88 ric impedances can be used to deduce the morphology and distribution of  
89 the CBD within the electrode. In combination with microstructure-resolved  
90 simulations, this approach was able to provide a quantitative link between  
91 CBD properties and half-cell performance for beyond state-of-the-art elec-  
92 trodes with an areal capacity of above 7 mAh/cm<sup>2</sup>.

93  
94 In Section 2, we provide a description of the manufacture as well as a  
95 structural and electrochemical characterization of the electrodes. Three dif-  
96 ferent cathodes each with varying electrode densities (2.7, 3.0, and 3.3 g/cm<sup>3</sup>)  
97 and a similar mass loading of 43.6 mg/cm<sup>2</sup> are characterized by synchrotron  
98 tomography. The CBD distribution cannot be resolved in the tomography  
99 data due to a low contrast to the pore space, hence, we additionally collect  
100 EDX-spectra on a cross-cut of the electrode for a qualitative analysis of the  
101 CBD distribution in the bulk of the electrode. We then iteratively add the  
102 effects of binder migration to the virtual electrodes based on its agreement

103 to the experimental EIS data. A description of this procedure is given in  
104 Section 3. Half-cell (HC) discharge simulations are run on the same set of  
105 electrodes and are availed to corroborate the findings from impedance simu-  
106 lations (see Section 4). Finally, in Section 5, we summarise our findings.

107

## 108 **2. Experimental methods**

### 109 *2.1. Electrode preparation and cell assembly*

110 For the preparation of the composite positive electrodes, a suspension of  
111 the active material  $\text{LiNi}_{0.6}\text{Co}_{0.2}\text{Mn}_{0.2}\text{O}_2$  (NMC622 BASF), conductive addi-  
112 tives and polyvinylidene fluoride binder (PVDF, Solvay Solexis) in the weight  
113 ratio 93:3:4 was prepared in the solvent N-methylpyrrolidone (NMP, Sigma  
114 Aldrich). The ratio of the conductive additives carbon black (Super P Li) to  
115 graphite (C-ENERGY SFG 6 L) from Imerys (formerly Timcal) was chosen  
116 2:1 for the reasons described in previous work [1]. For the preparation of the  
117 suspension, the solid components were added to a  $1.7 \text{ dm}^3$  planetary mixer  
118 (Grieser, Germany) equipped with a cross bar stirrer (CS) and a butterfly  
119 stirrer (BS) and dry-mixed for 10 min before the first portion of the solvent  
120 was added. The mixture was kneaded for 20 minutes within a temperature  
121 range of  $48 \text{ }^\circ\text{C}$  to  $62 \text{ }^\circ\text{C}$  and at a rotational speed of 67 rpm and 506 rpm of  
122 the CS and BS, respectively, to result in a total solid content of 88.7 wt.-%.  
123 Further NMP was added in three portions and after each addition, a rota-  
124 tional speed of 88 rpm (CS) and 900 rpm (BS) was applied over a total period  
125 of 4.5 hours. This period can be subdivided into a second kneading phase of  
126 a duration of 1.5 hours at a solid content of 85 wt.-% and a following diluting  
127 phase. The final solid content was 74.9 wt.-%. The suspension was applied  
128 with a doctor blade (Elcometer, Germany) on a  $20 \mu\text{m}$  thick aluminium col-  
129 lector foil (Korff AG, Switzerland) fixed by a vacuum plate and the fim was  
130 dried on a heat plate. The average mass loading was  $43.3 \text{ mg cm}^{-2}$ . The  
131 electrode was calendered with a table calender (Sumet, Germany) to differ-  
132 ent densities of the composite of 2.8, 3.0, and  $3.3 \text{ g cm}^{-3}$ , respectively. From  
133 these electrodes samples, circular discs with a diameter of 1.2 cm correspond-  
134 ing to an area of  $1.13 \text{ cm}^2$  were punched and thoroughly dried for 16 h at  $130$   
135  $^\circ\text{C}$  under vacuum. For the preparation of half cells in an argon-filled glove  
136 box, they were mounted in 2016-type coin cells as working electrodes and  
137 combined with lithium foil as a counter electrode, glass microfibre (GF/A,  
138 Whatman) as a separator and 1.0 M  $\text{LiPF}_6$  in a mixture of ethylene carbonate

139 and ethylmethyl carbonate (ratio 3:7 by weight) with an additional 2 wt.-%  
140 of vinylene carbonate (BASF) as electrolyte. For impedance measurements,  
141 symmetrical 2016-type coin cells were assembled in the same way and with  
142 the same materials as described for the half-cells apart from the following  
143 deviation. As electrodes, two discs from the same electrode sample, one with  
144 a diameter of 1.2 cm and the other with a diameter of 1.6 cm, were used.  
145 The difference in diameter was chosen to ensure complete overlapping of the  
146 smaller electrode by the larger one.

## 147 *2.2. Structural characterization*

148 The microstructure-resolved simulations for the calculation of electro-  
149 chemical impedance spectra will be performed on the tomographic image  
150 data of those electrodes described in Section 2.1. Tomographic imaging  
151 was performed at the synchrotron X-ray facility BAMline (BESSYII, Berlin,  
152 Germany)[54]. A monochromatic X-ray beam was produced by a Si-W mul-  
153 tilayer monochromator. The energy was 25 keV and an energy resolution of  
154  $\Delta E/E = 10^{-2}$  was applied. The X-rays were converted into visible light using  
155 a cadmium tungstate scintillator screen. The field of view covered by the  
156 optical lens system in combination with a CCD-camera (PCO camera, 4008  
157  $\times$  2672 pixels) was  $1.8 \times 1.2 \text{ mm}^2$ . With an exposure time of 2.5 seconds,  
158 2200 projections were measured over an angular range of  $180^\circ$ . The size of  
159 a voxel in the reconstructed image is 438 nm. After reconstruction, a 16-bit  
160 grayscale image of the electrode was created. In order to perform the electro-  
161 chemical simulations, a binarization of the image data is necessary, i.e., the  
162 grayscale image has to be transformed into a binary image, where one phase  
163 shows the active material particles, and the other phase the union of pores,  
164 binder and additives. Note that, due to the low contrast, it is not possible to  
165 differentiate between the CBD and pore space, therefore, it will be added on  
166 a model basis later (see Section 3.1.). The binarization was done by global  
167 thresholding, i.e., every voxel with a value larger than the assigned threshold  
168 is allocated to the active material particles, and the remaining voxels to the  
169 CBD and pore space. The threshold is chosen such that the volume fraction  
170 of the active material calculated from the binarised image matches the vol-  
171 ume fraction determined from the weight ratio of the materials, their bulk  
172 densities and the density of the electrode, which results in 57.4 vol.-%. A 3D  
173 rendering of the resulting binarized image data is shown in Figure 1d).

174

175 Cross-sections of electrodes were generated by broad-beam argon ion  
176 milling (Hitachi IM4000Plus). Milling time was at least 2 h at an ion beam  
177 voltage of 5 kV. Scanning Electron Microscopy (SEM) and energy disper-  
178 sive X-ray spectroscopy mapping (EDX) was carried out using a LEO 1530  
179 VP microscope equipped with a Gemini thermal field emission column to  
180 investigate the morphology and the elemental distribution of the electrodes.  
181 SEM images were obtained with a secondary electron detector at accelerating  
182 voltages between 4 and 5 kV. Fluorine was used as tracing element for the  
183 presence of the PVDF binder. Due to the sample heterogeneity, EDX is not  
184 perfectly suited to determine absolute concentrations of certain elements,  
185 however, observation of relative changes of the count rate under constant  
186 conditions has turned out to be a feasible method for gathering reliable in-  
187 formation [17]. Nevertheless, the absolute values strongly depend on the  
188 measuring parameters and therefore this technique only allows a qualitative  
189 interpretation.

### 190 *2.3. Electrochemical characterization*

191 The galvanostatic tests were performed with a cell test system from  
192 BaSyTech GmbH (Germany). After assembling, the cells were allowed to  
193 rest for 24 hours. They were then formed by three consecutive, galvanostatic  
194 symmetric cycles at C/10 between 3.0 and 4.3 V. Subsequently, their dis-  
195 charge rate capability was investigated by consecutively executing three half  
196 cycles between 4.3 V and 3.0 V at a current density of 1 mA cm<sup>-2</sup>, 3 mA  
197 cm<sup>-2</sup>, 6 mA cm<sup>-2</sup>, 8 mA cm<sup>-2</sup>, 10 mA cm<sup>-2</sup> and 12 mA cm<sup>-2</sup>, respectively.  
198 After the discharge with 6, 8 and 10 mA cm<sup>-2</sup>, one additional cycle was  
199 performed at 1 mA cm<sup>-2</sup> to check the capacity retention. The charge rate  
200 was constantly 1 mA cm<sup>-2</sup> followed by a constant voltage step at 4.3 V to  
201 ensure complete delithiation of the cathode.

202  
203 The EIS measurements were preceded by an open-circuit voltage (OCV)  
204 period of 20 h, and were carried out within a frequency range of 10 mHz  
205 and 300 kHz with 10 points per decade and applying a sinusoidal potential  
206 amplitude of 10 mV. All measurements were recorded on a VMP-3 electro-  
207 chemical workstation (Biologic) and repeated at least three times to ensure  
208 results reproducibility.

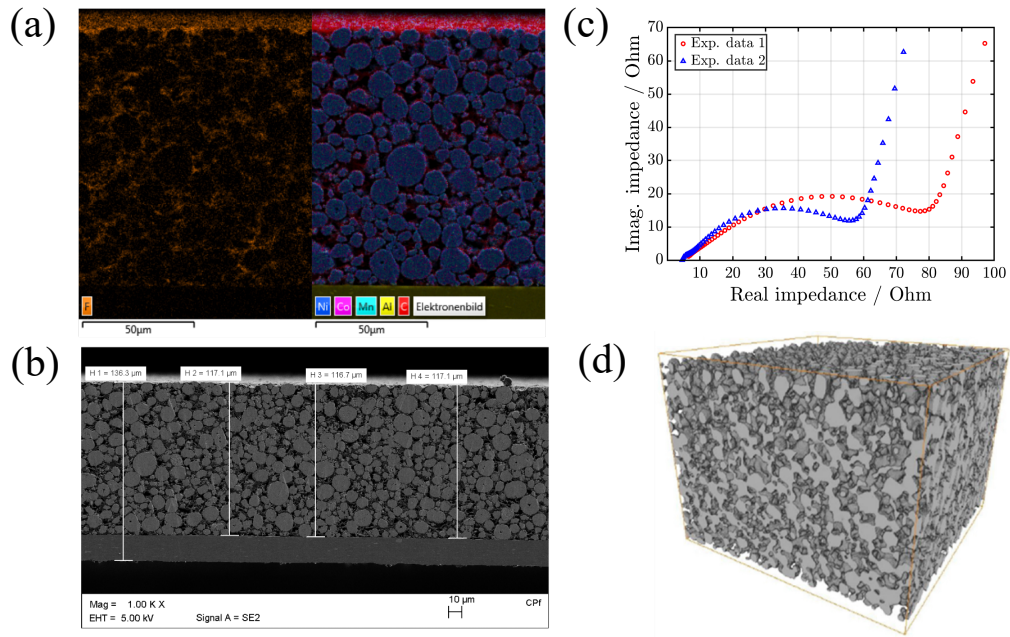


Figure 1: Segment (a) and (b) show SEM images of a cross-cut through an electrode with an areal capacity of  $5.7 \text{ mAh/cm}^2$  and a density of  $3.0 \text{ g/cm}^3$ . (a) includes in false-colour, information of EDX spectra representing different elements present in the cathode. (b) includes thickness measurements for the electrode coating and current collector. Impedance spectra measured in a symmetric cell setup under blocking electrolyte conditions for the electrodes with the same density and an areal capacity of  $7.3 \text{ mAh/cm}^2$  are given in (c), and a cutout of the binarized tomographic image data without CBD are presented in (d). Note: segments (a) and (b) are included for visual corroboration.

209 **3. Simulative methods**

210 In this section, we elaborate on the numerical methods employed; specif-  
211 ically shedding light on the generation of virtual electrodes by model-based  
212 insertion of the CBD, creation of domains with structural inhomogeneities,  
213 and the type of simulations conducted. A short description of the model and  
214 the corresponding parameters used is provided in Section 3.2. Additionally,  
215 the constitutive equations are summarized in Table II. Nomenclature can be  
216 found in Table SI-1 of the Supporting Information.

217 *3.1. Generation of virtual electrodes*

218 *3.1.1. Heterogeneous distribution of the CBD*

219 Three-dimensional reconstructions of the electrodes obtained from syn-  
220 chrotron tomography serve as a basis for the generation of the virtual elec-  
221 trodes. As it is challenging to conduct a reliable reconstruction of the CBD  
222 phase from tomographic data, it is distributed on a model-basis using an  
223 in-house structure-generator at the contact points of AM particles [31]. The  
224 EDX-mapping of an electrode cross-cut is shown in Figure 1 a). The re-  
225 sponse in orange in the left section of the image is due to the flourine in the  
226 PVDF binder, signaling binder enrichment towards the surface of the elec-  
227 trode. This is validated by the congruent distribution of carbon conductive  
228 additive (in red) in the conjoining image.

229 As outlined previously, binder enrichment at the electrode surface can  
230 cause i) a loss of preferred conduction pathways for electrons at the current  
231 collector and, ii) formation of a dense layer of CBD at the electrode surface,  
232 inhibiting lithium-ion penetration into the electrode. In order to isolate and  
233 study the effects of these two phenomena, the tomographic was appended  
234 to create five virtual electrodes, each representing differing scenarios of CBD  
235 spatial distribution. This is graphically elucidated in Figure 2.

236  
237 The five different configurations shown in Figure 2 have the corresponding  
238 physical prominence:

- 239 i) “No CBD at CC”: we describe the loss of electronic conduction pathways  
240 by assuming an extreme case, where a solid layer adjacent to the current  
241 collector is devoid of CBD (refer to the region in orange in Figure 2).  
242 The local effective electronic conductivity in this layer is given by that  
243 of NMC622.

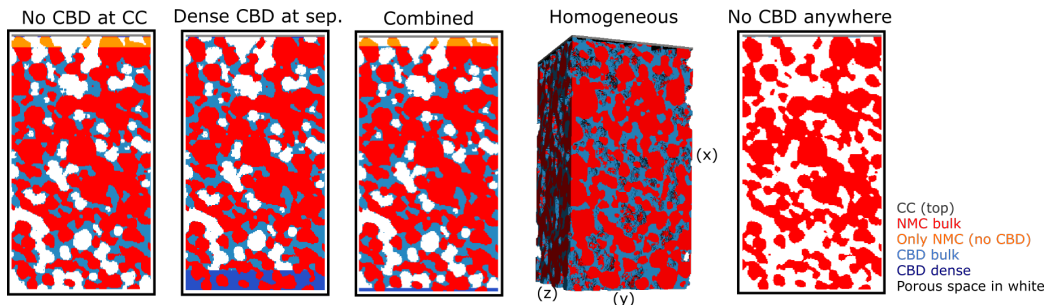


Figure 2: Illustrations of the different CBD configurations (2D slices are extracted at half the electrode thickness to enable better visualisation. An example in 3D is shown for the “Homogeneous” case). The current collector (CC) is shown at the top, and the porous space is given in white. The identifier for each configuration is listed above the respective image. Through-direction of transport between anode and cathode is denoted by  $x$ , whereas  $y$  and  $z$  are the in-plane coordinates. The dimensions of the electrodes are given in Table I.

- 244 ii) “Dense CBD at sep.”: binder enrichment at the electrode surface results  
 245 in a dense layer of accumulated CBD beside the separator (given in  
 246 dark blue).  
 247 iii) “Combined” is a combination of both the phenomena i) and ii); i.e.,  
 248 CBD-absent layers adjacent to the CC (in orange) and CBD-dense layers  
 249 adjacent to the separator (in dark blue).  
 250 iv) In “Homogeneous”, the CBD is distributed uniformly across the elec-  
 251 trode thickness.  
 252 v) Additionally, a fifth control configuration, “No CBD anywhere”, is stud-  
 253 ied, where the entire domain is devoid of any CBD material.  
 254

255 The width of the different layers in configurations i) through iii) is ad-  
 256 justed iteratively to reproduce the width of the real part of the impedance  
 257 measurements on symmetrical cells, i.e. the two minima of the real impedance  
 258 response (see Figure 6). It is to be noted, that the total volume fraction of  
 259 the CBD was not kept constant between the several configurations (refer to  
 260 Table SI-3 in the Supporting Information). Therefore, we can expect a qual-  
 261 itative prediction of the electrochemical performance measurements. Still,  
 262 these observations can give important insights on limiting processes owing to  
 263 heterogeneities in the electrode microstructure.

264 *3.1.2. Variation of electrode density*

265 The configurations representing the scenarios described in Section 3.1.1  
 266 are created for all electrode densities (2.7, 3.0 and 3.3 g/cm<sup>3</sup>). As calendering  
 267 alters the thicknesses of the CBD-absent/rich layers, these were iteratively  
 268 adjusted to match the impedance experiments. Refer to Table I and Table  
 269 SI-3 in the Supporting Information for sizes of the geometries.

270

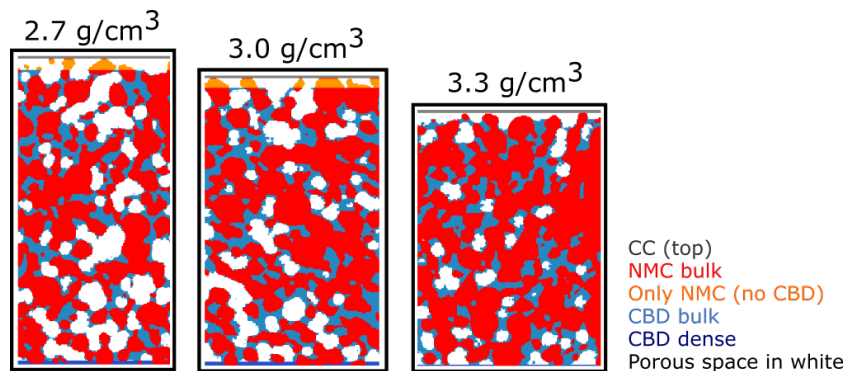


Figure 3: Phase distribution in representative 2D slices of the three different electrode densities for the “Combined” case. Increasing the electrode density compresses the solid structure, reducing the heterogeneously distributed CBD layers. This becomes evident when one compares the image of electrode with density 3.3 g/cm<sup>3</sup> with 2.7 g/cm<sup>3</sup>.

271 *3.2. Simulation framework and methodology*

272 All simulations presented in this article are performed with the develop-  
 273 ment branch of the **B**attery and **E**lectrochemistry **S**imulation **T**ool (BEST)  
 274 [55]. The simulations are able to provide the temporal and spatial distribu-  
 275 tion of lithium/ion concentration, potential, and temperature. Constitutive  
 276 equations are summarized in Table II and a detailed derivation is given in  
 277 [31, 50, 51]. To assist in the investigation of the influence of CBD distribu-  
 278 tion on the cell performance, we run symmetric cell EIS and HC galvanostatic  
 279 delithiation simulations. The cell setup for these two methods are shown in  
 280 the next sections.

281 *3.2.1. Electrode cutouts*

282 In order to account for the variations within the microstructure of the  
 283 electrodes arising from the processing steps, three non-overlapping cutouts

Table I: Thickness of layers with varying CBD content at all electrode densities. Configuration (i) is “No CBD at CC”, (ii) is “Dense CBD at sep.”, (iii) is “Combined”, and “Hom.” stands for “Homogeneous” case. The cross-section of the tomographic data is given by a quadrilateral with identical length ( $y$ ) and width. Thickness is given by  $x$ . The colours in brackets correspond to the regions in Figure 2.

Configuration	Hom.	(i)	(ii)	(iii)
2.7 g/cm <sup>3</sup>		$y = 74 \mu\text{m}; x = 152.9 \mu\text{m}$		
CBD absent (orange)	0	5.7	0	5.3
Bulk (blue)	152.9	147.2	138.9	141.8
CBD dense (dark blue)	0	0	14.0	2.2
3.0 g/cm <sup>3</sup>		$y = 79 \mu\text{m}; x = 141.9 \mu\text{m}$		
CBD absent (orange)	0	5.3	0	4.4
Bulk (blue)	141.9	136.6	130.6	134.9
CBD dense (dark blue)	0	0	11	2.6
3.3 g/cm <sup>3</sup>		$y = 83 \mu\text{m}; x = 116.9 \mu\text{m}$		
CBD absent (orange)	0	0.4	0	0.4
Bulk (blue)	116.9	116.5	111.6	116.1
CBD dense (dark blue)	0	0	5.3	0.4

Table II: The constitutive equations of the Li-ion battery model used in this work. Details of the derivation can be found in references [50, 51].  $\varepsilon$  in Equation 16 is 50%. For nomenclature, refer to the Supporting Information Table SI-1. Abbreviation “Elyte” stands for Electrolyte.

Phase	Material balance	Charge balance
Elyte	$\frac{\partial c_{\text{El}}}{\partial t} = -\vec{\nabla} \cdot \vec{N}_{\text{El}}$ (1)	$0 = -\vec{\nabla} \cdot \vec{j}_{\text{El}}$ (2)
AM	$\frac{\partial c_{\text{So}}}{\partial t} = -\vec{\nabla} \cdot \vec{N}_{\text{So}}$ (3)	$0 = -\vec{\nabla} \cdot \vec{j}_{\text{So}}$ (4)
Phase	Lithium flux	Charge flux
Elyte	$\vec{N}_{\text{El}} = -D_{\text{El}} \vec{\nabla} c_{\text{El}} + \frac{t_{\pm}}{F} \vec{j}_{\text{El}}$ (5)	$\vec{j}_{\text{El}} = -\kappa_{\text{El}} \vec{\nabla} \varphi_{\text{El}} + \kappa_{\text{El}} \frac{1-t_{\pm}}{F} \left( \frac{\partial \mu_{\text{El}}}{\partial c_{\text{El}}} \right) \vec{\nabla} c_{\text{El}}$ (6)
AM	$\vec{N}_{\text{So}} = -D_{\text{So}} \vec{\nabla} c_{\text{So}}$ (7)	$\vec{j}_{\text{So}} = -\sigma_{\text{So}} \vec{\nabla} \Phi_{\text{So}}$ (8)
Interface	Lithium flux	Charge flux
Elyte	$\vec{N}_{\text{El}} = N_{\text{El}} \cdot \vec{n}_{\text{A}} = \frac{i_{\text{BV}} + i_{\text{DL}}}{F}$ (9)	$\vec{J}_{\text{El}} = J_{\text{El}} \cdot \vec{n}_{\text{A}} = i_{\text{BV}} + i_{\text{DL}}$ (10)
AM	$\vec{N}_{\text{So}} = N_{\text{So}} \cdot \vec{n}_{\text{A}} = \frac{i_{\text{BV}}}{F}$ (11)	$\vec{J}_{\text{So}} = J_{\text{So}} \cdot \vec{n}_{\text{A}} = i_{\text{BV}} + i_{\text{DL}}$ (12)
	Faraday current: $i_{\text{BV}} = i_0 \left[ \exp\left(\frac{\alpha F}{RT} \eta\right) - \exp\left(\frac{(1-\alpha)F}{RT} \eta\right) \right]$ (13)	
	Double layer current: $i_{\text{DL}} = -C_{\text{DL}} \cdot \frac{d}{dt} (\Phi_{\text{So}} - \varphi_{\text{El}})$ (14)	
Elyte - AM	$i_0 = i_{00} c_{\text{El}}^{\alpha} c_{\text{So}}^{(1-\alpha)}$ ; $\eta = \Phi_{\text{So}} - \varphi_{\text{El}} - U_0(c_{\text{So}})$ (15)	
Elyte in CBD - AM	$i_{\text{eff}} = \varepsilon i_0$ ; $\eta = \Phi_{\text{So}} - \varphi_{\text{El}} - U_0(c_{\text{So}})$ (16)	
Elyte - Li	$i_0 = i_{00} c_{\text{El}}^{\alpha}$ ; $\eta = \Phi_{\text{So}} - \varphi_{\text{El}}$ (17)	

284 with the same dimensions in the in-plane direction and the complete thick-  
 285 ness in the through-plane direction are assessed. This approach additionally  
 286 provides statistical information on structural fluctuations on the length scale  
 287 of a few micrometers.

### 288 3.2.2. Virtual cells

289 The virtual cells either consist of a separator and two identical NMC622  
 290 electrodes or an NMC622 electrode with a lithium-metal anode corresponding  
 291 to the symmetrical cell and HC setup, respectively (Figure 4). Each electrode  
 292 is in contact with the current collector. The cathodes were embedded with  
 293 up to six voxels in the current collector to ensure good contact and numerical  
 294 convergence. A summary of the parameters and properties used for each of  
 295 these simulations is provided in Table SI-1 of the Supporting Information.

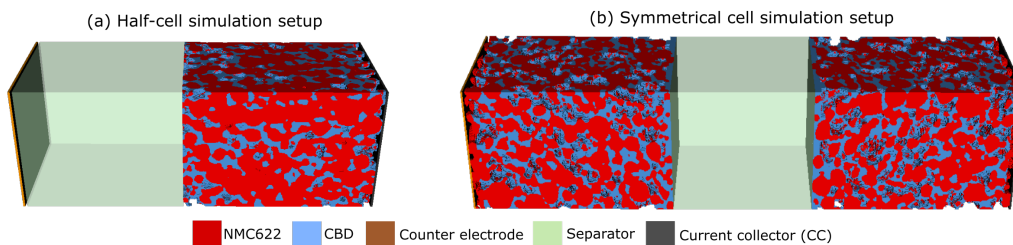


Figure 4: Simulation setups for a (a) HC galvanostatic lithiation of the cathode and (b) electrochemical impedance spectroscopy in symmetric cell configuration. The pore space is transparent.

### 296 3.2.3. Separator

297 The separator is modelled as a porous membrane of 10  $\mu m$  thickness,  
 298 comprising of 50% electrochemically inactive material. The bulk electrolyte  
 299 is assumed to occupy the pore spaces homogeneously.

### 300 3.2.4. Bulk electrolyte

301 In the electrolyte, the concentration and electrochemical potential of  
 302 lithium ions is solved for by the conservation equations for mass and charge,  
 303 given by Equations (1) and (2) in Table II, respectively. The bulk electrolyte  
 304 transport parameters used for  $LiPF_6$  in EC/EMC at 298  $K$  (ionic conductiv-  
 305 ity, transference number, diffusion coefficient, thermodynamic factor) are  
 306 as measured by Nyman *et al.* [56].

307 *3.2.5. Lithium anode*

308 The lithium anode is modelled as a 1.31  $\mu\text{m}$  long flat electrode with an  
309 infinite source of lithium available for intercalation at the cathode. The kinet-  
310 ics constants are calibrated against literature data [57] reported in previous  
311 work [1].

312 *3.2.6. Cathode active material*

313 At the interface of the active material and electrolyte, we describe the  
314 intercalation reaction of lithium-ions by a Butler-Volmer type equation (13)  
315 and additionally consider contributions of the electric double-layer (14) in  
316 parallel to the Faradaic current. The double-layer has a constant areal ca-  
317 pacity and is modelled as a parallel plate capacitor. The coupling conditions  
318 at the interface between the active material and the electrolyte are given by  
319 Equations (9) - (12). The concentration of lithium ( $c_{\text{So}}$ ) in the active ma-  
320 terial can be calculated by solving the corresponding conservation equation  
321 of mass given by Equation (3). Finally, an additional equation for the cal-  
322 culation of the electric potential in the solid phase is required. At the AM  
323 and CBD solid subdomain interface, the model allows for a continuous flow  
324 of electrons, thereby accounting for the influence of the CBD distribution on  
325 the electronic conductivity of the AM particles. The conservation of charge is  
326 given by Equation (4) and the flux of electrons is calculated as per Equation  
327 (8). The fit data for the chemical diffusion coefficient ( $D_{\text{So}}$ ) and electronic  
328 conductivity ( $\sigma_{\text{So}}$ ) as a function of the  $c_{\text{So}}$  is given in [58].

329 *3.2.7. CBD*

330 As previously mentioned, the CBD is distributed on a model-basis at the  
331 contact points of AM particles, and is assumed to have an isotropic porosity  
332 of 50%, that allows ion conduction. The effective ion transport is given by  
333 the effective tortuosity values as determined in [45] for a two-layer electrode  
334 with a total CBD volume fraction of 11.54 vol-%, compared to 11.2-vol-%  
335 (before calendaring) used in this study. The two-layered electrodes show-  
336 cased a more gradual binder distribution gradient, as the two layers were  
337 inherently manufactured with different suspensions. Hence, the effective tor-  
338 tuosity factor for a two-layer electrode, where the CBD is placed based on a  
339 morphological closing of the active material that takes the EDX information  
340 into account, was chosen.

341

342 This factor was applied in this study as a function of the CBD distribu-  
 343 tion. In the bulk of the electrode,  $\kappa_{CBD_{Bulk}} = 0.12 \cdot \kappa_{Electrolyte_{Bulk}}$  [45], where  $\kappa$   
 344 is used to describe ionic conductivity. At the separator, due to the enrichment  
 345 of the polymeric binder and its role in impeding ion transport, this factor  
 346 is set to be higher (see Figure 5), i.e.  $\kappa_{CBD_{Dense}} = 0.1 \cdot \kappa_{CBD_{Bulk}}$ . Once the  
 347 effective transport properties are defined, the conservation equations for elec-  
 348 trolyte transport (Equations (1) and (2)) are solved to determine the lithium  
 349 ion concentration within the CBD pore network. At contact points between  
 350 the AM and CBD, the specific active electrolyte surface area is reduced to  
 351 50% (proportional to CBD porosity), downscaling the AM-Electrolyte inter-  
 352 calation and double-layer kinetics at these points by the same factor (see  
 353 Equation (16)). Note, that there are no chemical reactions modelled at the  
 354 interface of the solid fraction of the CBD and the liquid electrolyte.

355 Finally, the electric transport in the CBD solid subdomain is deter-  
 356 mined by the conservation Equations (4) and (8). Figure 1 shows that there  
 357 is also an aggregation of the conductive additive at the electrode surface  
 358 ( $\sigma_{CBD_{Dense}}$ ), thereby increasing the electronic conductivity in these layers.  
 359 Hence,  $\sigma_{CBD_{Dense}} = 2 \cdot \sigma_{CBD_{Bulk}}$ . At the CBD and AM solid interfaces, the  
 360 model allows for a continuous flow of electrons.

361

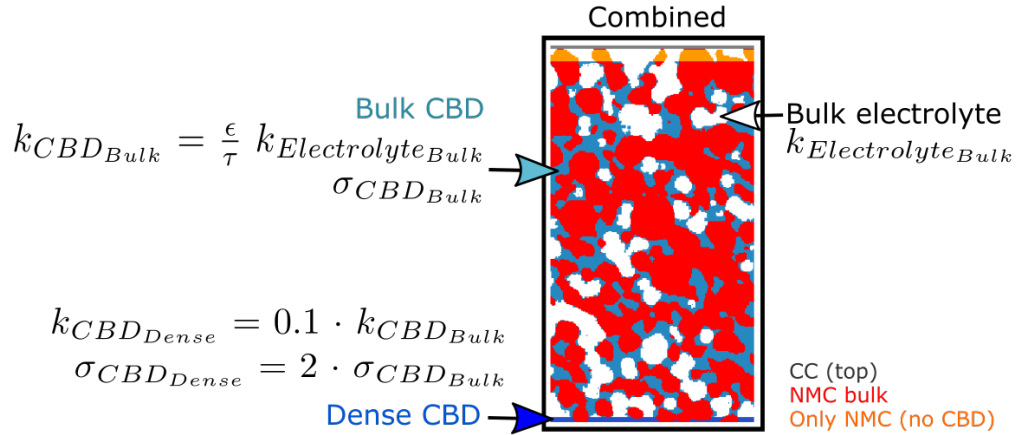


Figure 5: Effect of heterogeneous CBD distribution on the effective transport parameters in different phases illustrated for a “Combined” configuration.

362 *3.3. Electrochemical simulations*

363 All electrochemical simulations, including effective conductivity, are run  
364 on the same set of virtual electrodes, in order to deconvolute the effect of  
365 binder distribution on the electrode performance. A detailed description of  
366 the methodology for the calculation of impedance spectra can be found in  
367 our previous publications [31, 59].

368 *3.3.1. Effective conductivities*

369 The effective conductivities of each of the configurations for all elec-  
370 trode densities are solved for numerically. The steady-state Poisson equation  
371 (Equation 18) is solved with a constant current density boundary condition  
372 (as elucidated in [43]). The potential distribution then takes into account  
373 the differing effective conductivities of the various materials in the electrode.  
374 Note, that the calculations are performed separately for the solid (solid CBD  
375 fraction + cathode AM) and liquid phase (porous CBD fraction + bulk elec-  
376 trolyte). Refer to Section 3.2 of the Supporting Information sheet for the  
377 effective electronic and ionic conductivities of the electrodes at differing elec-  
378 trode densities and CBD distributions.

$$\sigma_{effective} = j \frac{\Delta x}{\Delta \phi} \quad (18)$$

379 *3.3.2. Electrochemical Impedance Spectroscopy (EIS)*

380 The impedance spectra are calculated by the potential-step and current  
381 relaxation technique [60] for symmetric cells under steady-state. A detailed  
382 description is provided in our previous publication [31]. Starting in a steady-  
383 state, we excite the cell with a small potential step of 2 mV, and monitor  
384 the resulting current signal. Finally, the impedance at different frequencies  
385 is evaluated by dividing the Fourier transform [61] of the voltage with the  
386 current signal. Furthermore, symmetric cells (in comparison to HCs) provide  
387 the advantage that one can isolate the response due to a single electrode  
388 chemistry, without it being mangled by a counter electrode. The results of  
389 these simulations are presented in Section 4.1.

390 In the experiments, the cells are subjected to blocking electrolyte con-  
391 ditions, resulting in an ideally polarisable electrode where a current is only  
392 induced by capacitive effects. Blocking conditions in the simulations are  
393 achieved by setting the cathode AM potential close to complete lithiation,  
394 resulting in low ion intercalation at the AM and electrolyte interface and,  
395 correspondingly, low AM electronic conductivity.

396 *3.3.3. Galvanostatic discharge*

397 Half-cell (HC) galvanostatic delithiation (of the anode) simulations are  
398 run with lithium metal as the counter-electrode. The initial lithiation degree  
399 of the electrodes is set to correspond to a cell voltage of 4.3V, following the  
400 experimental conditions. In all simulations, we start with a homogeneous  
401 initial concentration of lithium in the active material, and lithium ion in the  
402 electrolyte. All virtual electrodes of different electrode densities were dis-  
403 charged with current densities of 1.5, 3.0, 6.0 and 12 mA/cm<sup>2</sup> down to a  
404 lower cut-off voltage of 3.0 V. Results of the HC simulations are presented  
405 in Section 4.2.

406

## 407 4. Results and Discussion

408 The results of the electrochemical methods discussed above are presented  
409 in this section. The connection between microstructural heterogeneities and  
410 the cell performance can be established via symmetric cell EIS. More specif-  
411 ically, we use the EIS data to qualitatively inform the different scenarios  
412 of CBD distribution by comparing experiment and simulation. In a next  
413 step, we simulate HC discharge phenomena on the same 3D microstructure-  
414 resolved geometries. Hence, this section is divided into two parts: first, we  
415 dive into the results of the impedance spectra simulations and finally, we  
416 corroborate this data with HC delithiation simulations at different discharge  
417 currents. The initial conditions and material parameters applied are iden-  
418 tical for all impedance simulations. Hence, the reason for the differences in  
419 responses is exclusively due to structural variations in the CBD distribution.

### 420 4.1. Symmetric cell impedance spectra

421 In this section, we will analyse the impedance responses of (i) different  
422 CBD structural scenarios firstly for the  $3.0 \text{ g/cm}^3$  density electrode and then  
423 (ii) under varying electrode densities, and compare them to experimental  
424 data. There were two EIS measurements per electrode, marked in gray as  
425 Exp. Data 1 and 2 in Figure 6. For the sake of clarity, unless otherwise men-  
426 tioned, all the results shown in the upcoming sections are restricted to one  
427 representative electrode cutout only. The data regarding all three cutouts of  
428 the segmented tomographic image data is provided in Section SI 4.2.1. of the  
429 Supporting Information. We start with a short analysis of the experimental  
430 measurements before introducing the simulated data.

431 *4.1.1. Effect of structural scenarios*  
 432 *Experimental data.*

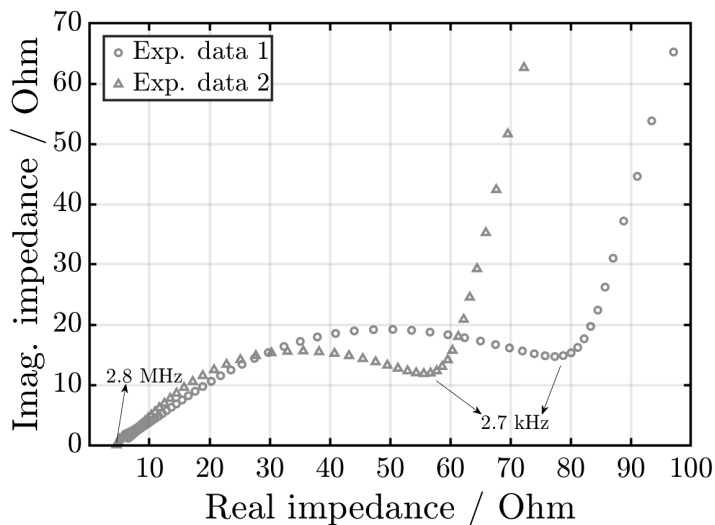


Figure 6: Nyquist plot of EIS measurements conducted under blocking conditions in a symmetrical cell setup. The figure shows the high-frequency data of measurements on two electrode samples with density  $3.0 \text{ g/cm}^3$ . The abbreviation “Exp.” stands for experimental data.

433

434 Figure 6 shows the results for impedance measurements of a symmetrical  
 435 cell under blocking conditions for a  $3.0 \text{ g/cm}^3$  density electrode. Under ideal  
 436 conditions (uniform electronic and ionic conductivities across the electrode),  
 437 we expect a linear increase of the imaginary part in a 45 degree angle to the  
 438 real axis [31, 32]. However, in our measurements, we observe two character-  
 439 istic regions: a high frequency region ( $> 2000 \text{ Hz}$ ), and a region with linear  
 440 increase region of the imaginary part. The indicated frequency ranges are  
 441 not consistent with the typical values reported for charge-transfer kinetics  
 442 at the interface of AM and electrolyte. In the next section, we show how  
 443 this phenomenon can be reproduced due to structural heterogeneities in the  
 444 electrode.

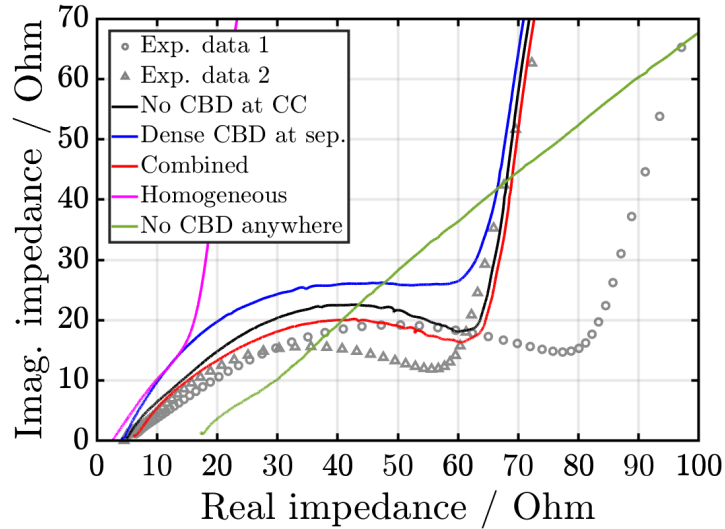


Figure 7: Nyquist plot of EIS measurement and simulation data of electrodes with density of  $3.0 \text{ g/cm}^3$  in a symmetric cell configuration. Simulations performed on the same 3D reconstruction with different CBD distribution are represented by solid lines. Simulation labels correspond to the configurations illustrated in Figure 2. Both the simulation (in solid lines) and experiments (in gray markers) were conducted under blocking conditions. The abbreviation “Exp.” stands for experimental data.

446

447 Figure 7 shows the impedance spectra of symmetric cells from the simu-  
 448 lations (in solid lines) alongside the experimental data (marked by symbols).  
 449 Reference configurations with a homogeneous CBD distribution or the “No  
 450 CBD anywhere” case show expected trends, namely a linear increase of the  
 451 imaginary part in the first region of the spectra. However, in the “Homoge-  
 452 neous” case, the width of the real part of the impedance is smaller compared  
 453 to the experimental data, and the scenario without any CBD has an order of  
 454 magnitude higher impedance. This emphasises the relevance of the electronic  
 455 network.

456 As elucidated before, the thicknesses of the respective heterogeneous lay-  
 457 ers in the various scenarios were adjusted so as to closely match the real  
 458 part of the experimental impedance (i.e. the width of the semi-circle from

459 the first intercept where the imaginary part is zero, to the second minima  
460 of the imaginary impedance). Since the semi-circle occurs at such large fre-  
461 quencies, it highlights the faster processes occurring in the electrode, such  
462 as the electron transport within the solid matrix controlled by the inherent  
463 conductivities and connectivities of the solid CBD and cathode AM, and  
464 ion transport within the pore space. Hence, both the absence or dense ac-  
465 cumulation of the CBD promotes regions of high potential gradients in the  
466 solid and electrolyte phase. The high frequency semi-circle is, therefore, only  
467 prominent in configurations that have some heterogeneity in the CBD dis-  
468 tribution, indicating such microstructural non-uniformities to be present in  
469 the real electrodes studied here.

470 A distribution of these potentials across the electrodes leads to varying  
471 degrees of dominance of either the ionic or electronic current with respect to  
472 time. Looking at the individual cases more specifically, the “Dense CBD at  
473 sep.” has binder enrichment at the electrode surface, and hence, presents a  
474 constriction to ion transport. As the number of accumulated CBD layers at  
475 the separator required to mimick the impedance data is much larger than the  
476 number with poor electronic connection to the CC (seen from Table I), the  
477 “Dense CBD at sep.” case has a higher total impedance at shown frequencies  
478 when compared to the “No CBD at CC” case. Combining both the effect of  
479 absent CBD at the CC in “No CBD at CC”, and the enriched layers in “Dense  
480 CBD at sep.”, gives the “Combined” scenario which best agrees with the  
481 experimental data. This configuration is also able to mimic the flatter semi-  
482 circle as seen in the experiments. This is an indication that the “Combined”  
483 case is most representative of electrodes studied in this work, however overall,  
484 the impedance spectra of the heterogeneous electrodes qualitatively match  
485 the experimental data. The imaginary part of the spectra is slightly more  
486 prominent in the simulations, owing to the qualitative nature of the study.  
487 For further insight into the corresponding effective transport parameters of  
488 the studied structures, refer to Section SI 3.2. of the Supporting Information.

489 In order to ensure that the high-frequency semi-circle behaviour was not  
490 an artefact of the kinetics and bulk CBD transport properties employed in  
491 the model, further parallel studies were conducted with varying kinetic con-  
492 stants and bulk CBD transport coefficients. There were no variations in this  
493 behaviour when the intercalation constant or double-layer capacitances were  
494 changed by a factor of 10% in either direction (see Section SI 4.1. in the  
495 Supporting Information). Moreover, the chosen bulk CBD transport param-  
496 eters did not alter the 45 degree angle response of the “Homogeneous” case.

497 Hence, we can deduce that the high-frequency semi-circle is indeed a product  
 498 of structural heterogeneities due to the CBD distribution.

499 In summary, microstructural defects within the electrode matrix causes an  
 500 inhomogeneous polarisation of the electrode, leading to an additional semi-  
 501 circle in the impedance spectra at frequencies higher than the characteristic  
 502 frequencies typical of charge transfer kinetics. We could demonstrate that  
 503 the experimentally prepared electrodes have both electronically limiting (low  
 504 amount of conductive carbon at the CC), and ionically limiting (dense binder  
 505 phase at the separator) heterogeneities, where the former is more dominat-  
 506 ing. The “Homogeneous” scenario shows the lowest impedance, hence it is  
 507 expected to perform best at all HC discharge currents, while the “Combined”  
 508 scenario is expected to be in line with the experimental data. Therefore, we  
 509 will restrict ourselves to the latter configuration when comparing the effect  
 510 of electrode calendering on the impedances in the next section.

511 *4.1.2. Effect of calendering*

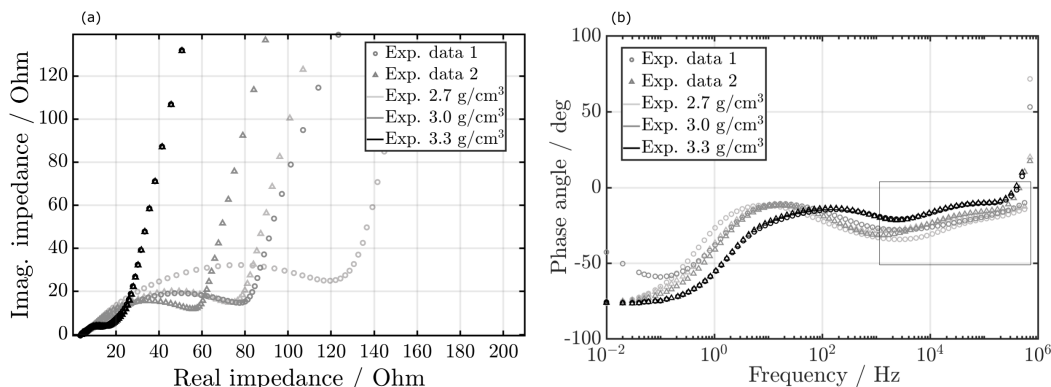


Figure 8: Impedance measurements on electrodes in a symmetric cell configuration. Different shades of grey indicate variations in electrode density between 2.7 and 3.3 g/cm<sup>3</sup>. For each density we performed two measurements. (a) Nyquist plot of impedance spectra showing the high-frequency semi-circle. (b) corresponding phase angle plots for the experimental data on electrodes with densities 2.7, 3.0 and 3.3 g/cm<sup>3</sup>. The experiments were conducted under blocking conditions. The abbreviation “Exp.” stands for experimental data.

512 *Experimental data.* Figure 8 (a) shows the symmetric cell impedance mea-  
 513 surements under blocking conditions on electrodes with densities of 2.7, 3.0  
 514 and 3.3 g/cm<sup>3</sup>. The darker the gray shade, the higher the electrode density.

515 With increasing calendering rate or electrode density, the width of the high-  
516 frequency semi-circle decreases. Calendering of the electrodes enhances the  
517 electronic contact between the conducting solid particles themselves and the  
518 CC, while reducing the porosity and increasing the pore transport resistance.  
519 This process not only compresses the bulk electrode, but also the layers  
520 with heterogeneities in the CBD fraction, thereby decreasing the impedance  
521 registered by the high-frequency semi-circle with an increase in calendering  
522 density. This decrease of the impedance indicates that both a CBD defi-  
523 cient layer and a CBD rich layer are present, however the former dominates  
524 the electrode impedance. Impedance spectra at higher electrode densities  
525 are close to the ideal behaviour of the homogeneous electrode, and show a  
526 lower standard deviation between the cutouts. This is also paralleled by the  
527 simulations.

528 *Simulation results.* Figure 9 shows the impedance response for the three elec-  
529 trode densities under the “Combined” scenario along with the corresponding  
530 experimental data. Simulation results of the other scenarios are reported  
531 in the Supporting Information (see Section SI 4.2.1.). The three lines for  
532 each electrode density represent the three cutouts from different regions of  
533 the electrode. In all cases, the thicknesses of the heterogeneous layers was  
534 adjusted to reproduce the experimental data, while retaining the same total  
535 electrode thickness. Refer to Table I for data on the average dimensions.

536 Consistent with the experimental data, the higher density electrodes ex-  
537 hibit a smaller impedance in the high-frequency region. As seen in Table I,  
538 the number of enriched and absent CBD layers are thinner at higher elec-  
539 trode densities. This leads to fewer regions of large potential jumps in the  
540 electrode, and hence, a lower electrode polarisation. Also, simulations on  
541 electrodes with low electrode density consistently reproduce the experimen-  
542 tal data, including the aspect of higher standard deviation between the three  
543 cutouts.

544 In the next section, we attempt to corroborate the impedance results  
545 summarised in the previous sections with the HC discharge data.

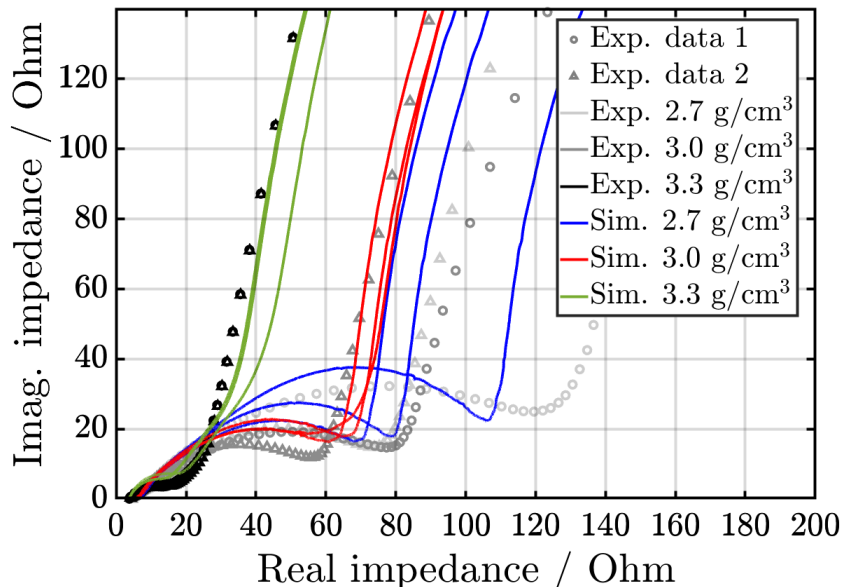


Figure 9: Nyquist plot of EIS data from simulation (solid lines) and experiment (symbols) under blocking conditions. Different colors indicate simulations on 3D reconstructions for the “Combined” scenario with different electrode density. For each density we performed three simulations on three cutouts highlighting the heterogeneity detected in image data. Corresponding measurement data is included as open symbols in the graph and also shown in Figure 8. The abbreviations “Exp.” and “Sim.” stand for experimental data and simulation results, respectively.

546 *4.2. Galvanostatic delithiation*

547 The galvanostatic discharge simulations were conducted at 4 different  
 548 discharge currents: 1.5, 3.0, 6.0 (approximately 1C), and 12 mA cm<sup>-2</sup>. This  
 549 was done for the various structural scenarios, electrode densities and cutouts  
 550 of the tomographic image data. For clarity, unless otherwise specified, all  
 551 the results presented here are for one cutout only. For insight into all the  
 552 data, we direct the interested reader to the Supporting Information (see  
 553 Section 4.2.2.). The discharge curves are simulated in the voltage window  
 554 between 4.3V and 3.0V. The results for the mid-density electrode at 1C will  
 555 be discussed first, before addressing the effect of changing C-rates. Finally,  
 556 we will discuss the influence of calendaring on delivered electrode capacities.

557 *4.2.1. Effect of structural scenarios at 1C*

558 The discharge curves at  $6 \text{ mA cm}^{-2}$  for the electrode with  $3.0 \text{ g/cm}^3$   
 559 density are shown in Figure 10. The curve marked gray represents the ex-  
 560 perimental data, while those in solid colours are simulated results.

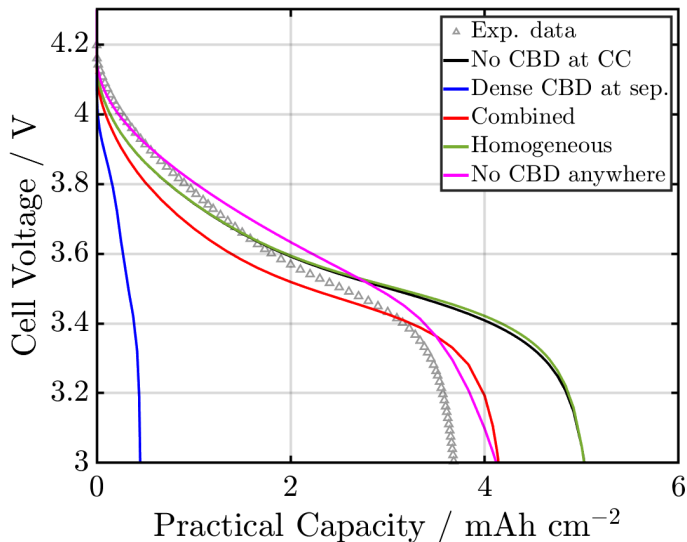


Figure 10: Results of HC discharge simulations on electrodes with density  $3.0 \text{ g/cm}^3$ . Discharge is simulated between 4.2 and 3.0 V with constant discharge current density of  $6 \text{ mA cm}^{-2}$ . Solid lines with different colours represent simulation data of different CBD configurations introduced in Figure 2. Measurements at the same discharge current are given by gray triangles.

561 As expected, the areal capacity of the “Homogeneous” electrode is the  
 562 highest, retaining about 80% of its capacity from  $1.5 \text{ mA/cm}^2$ . At this cur-  
 563 rent density, the benefit of both highly conductive electronic networks and  
 564 ionic pathways is evident. The “Homogeneous” scenario can also be regarded  
 565 as the benchmark for the other scenarios.

566 The “No CBD at CC” scenario performs almost on par with the “Ho-  
 567 mogeneous” case, even though the impedance in the symmetrical cell setup  
 568 was significantly larger for the former. Except for the CBD-absent layer,  
 569 the backbone electrode microstructure is identical to the “Homogeneous”  
 570 scenario (due to this similarity, the subsequent distributions for the “Homo-  
 571 geneous” case are not redundantly shown). This indicates that small layers  
 572 of poor electronic contact to the CC do not significantly affect discharge ca-

573 pacities. Interestingly, the scenario “No CBD anywhere”, shows remarkable  
574 electrochemical performance despite very poor effective electronic conduc-  
575 tivity. Furthermore, this scenario agrees best with the experimental data.  
576 However, this is clearly not the most probable scenario either in our study,  
577 or practically. This demonstrates that ionic transport is the decisive process  
578 determining the capacity of the cell, atleast at this current density. The  
579 scenario with a dense CBD at the separator represents the extreme case  
580 of lithium-ion transport limitations. In this case, we observe a significant  
581 loss in capacity, underlining the impact of inhomogeneous CBD distribution  
582 on lithium-ion transport and performance. Although in qualitative agree-  
583 ment with impedance data, the two extreme scenarios “No CBD at CC”  
584 and “Dense CBD at sep.” either over- or underestimate the discharge ca-  
585 pacity. Hence, we conclude that the combination of the two indeed provides  
586 the most realistic scenario to reproduce both the impedance and lithiation  
587 experiments. This can be better visualised in Figure 11.

588 Figure 11 shows the state-of-charge (SoC) distribution within the cathode  
589 AM for four chosen configurations. In the “No CBD anywhere” scenario,  
590 the overpotential for intercalation at the CC is lowest, due to poor electronic  
591 connection to the bulk electrode, resulting in a low AM SoC in this region.  
592 On the contrary, the “Dense CBD at sep.” scenario showcases a higher AM  
593 SoC at the separator. The ion transport is restricted to the few larger pores  
594 connected to the separator, as there is an impediment to transport into the  
595 bulk electrode pore space due to the binder enrichment. This is also promi-  
596 nent in the “Combined” case. The lithium-ion flux across the separator for  
597 the “Combined” case is higher than for the “Dense CBD at sep.” case due to  
598 the thinner accumulated binder. This is well-visualised in Figure 12, which  
599 shows the lithium-ion flux across the electrode. It is clear, that the lithium-  
600 ion transport preferentially occurs in the mesoporous space due to the high  
601 ion transport tortuosity in the porous CBD. The obvious advantage of acces-  
602 sible porous volume for ion transport into the electrode is demonstrated by  
603 the “No CBD anywhere” scenario, reflected in its relatively high discharge  
604 capacity.

605 We shall now look into how changing the discharge current density affects  
606 the transport in these various scenarios.

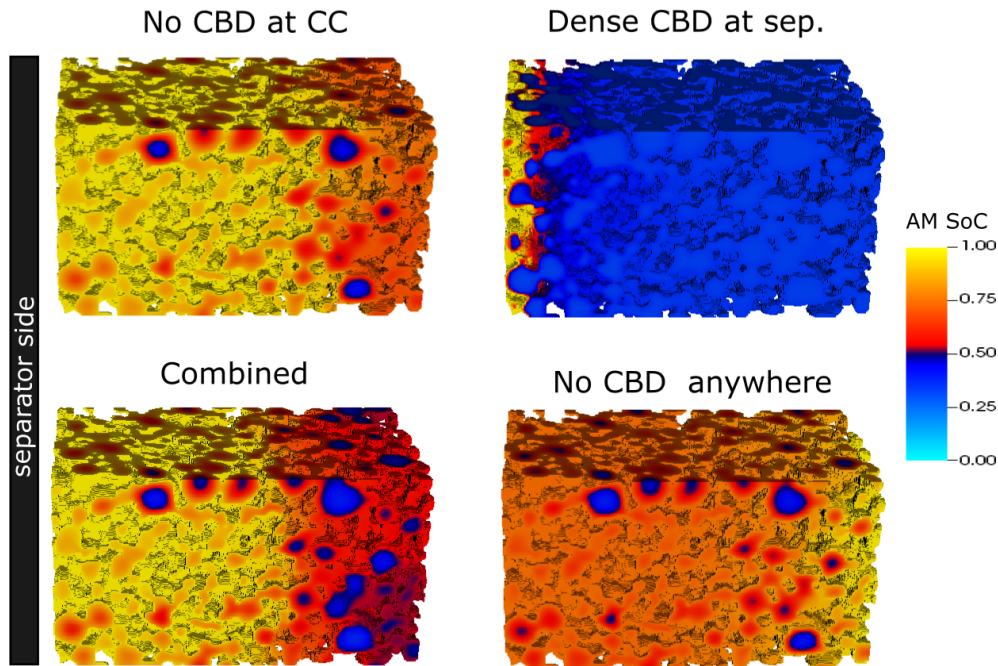


Figure 11: 3D distribution of the cathode AM state-of-charge (SoC) representing the normalized lithium distribution in an electrode with a density of  $3.0 \text{ g/cm}^3$  at the lower cut-off (3.0 V) of a lithiation simulation with  $6 \text{ mA/cm}^2$  constant current. Different panels represent the scenarios introduced in Figure 2. The separator is on the left hand side of the 3D distribution in each panel and the current collector is to the right.

607 *4.2.2. Effect of discharge current density*

608 Figure 13 shows the discharge areal capacity of the different configurations  
 609 at increasing current densities for the electrode with a density of  $3.0 \text{ g/cm}^3$ .  
 610 In this graph, we present the average discharge capacities of all three electrode  
 611 cutouts, normalised to their nominal capacity value (done the same way for  
 612 the experimental data points). The triangular marker in gray represents the  
 613 experimental data. The nominal capacity values for all the electrodes and  
 614 their cutouts can be found in the Supporting Information (see Table SI-4).

615 All scenarios show the expected drop in capacity with increasing dis-  
 616 charge current. The scenario with a homogeneous CBD distribution, serving  
 617 as a benchmark in our study, provides the highest capacity up to currents  
 618 of  $6 \text{ mA/cm}^2$ . Interestingly, the hypothetical scenario without any CBD  
 619 anywhere shows the highest capacity at the highest current, in-turn also sig-  
 620 nificantly overestimating the capacity compared to experiments. This sheds

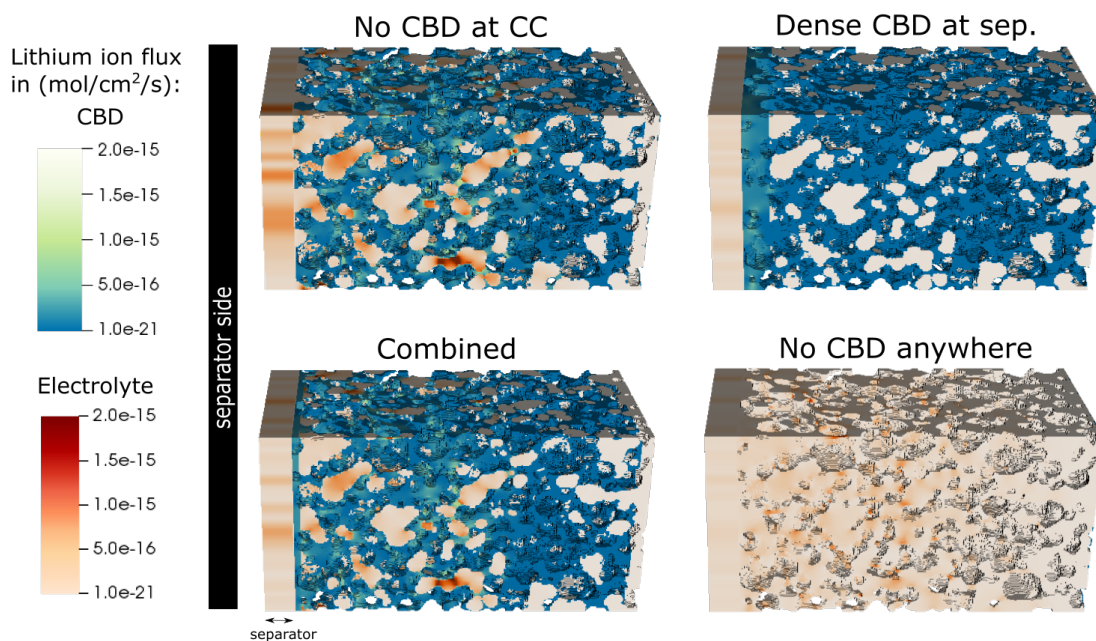


Figure 12: Flux of lithium ions within the pore space of an electrode with a density of  $3.0 \text{ g/cm}^3$ . Different panels represent the scenarios introduced in Figure 2. The separator is on the left hand side of the 3D distribution in each panel and the current collector is to the right. The color scales indicates the flux of lithium ions in the electrolyte within the mesopores (orange colour scale) and CBD (blue colour scale) at the lower cut-off voltage  $3.0\text{V}$  after lithiation with a constant current of  $6 \text{ mA/cm}^2$ . The active material is transparent.

621 light on the limiting effect of ion transport on battery performance, especially  
 622 at higher discharge currents.

623 The “No CBD at CC” scenario performs on par with the “Homogeneous”  
 624 case at all current densities, showing only smaller capacities at low current  
 625 densities due to its poor electronic conduction at the CC. In contrast, the  
 626 scenario with a dense CBD accumulation at the separator causes a rapid loss  
 627 of capacity with increasing current. Thereby significantly over-predicting  
 628 the influence of transport limited ions in the electrolyte. As previously sur-  
 629 mised, the “Combined” scenario demonstrates the best agreement with the  
 630 experimental data.

631 This further corroborates our understanding that the electrodes investi-  
 632 gated in this work have both electronically and ionically non-uniform net-  
 633 works and that this distribution critically affects the electrode performance.

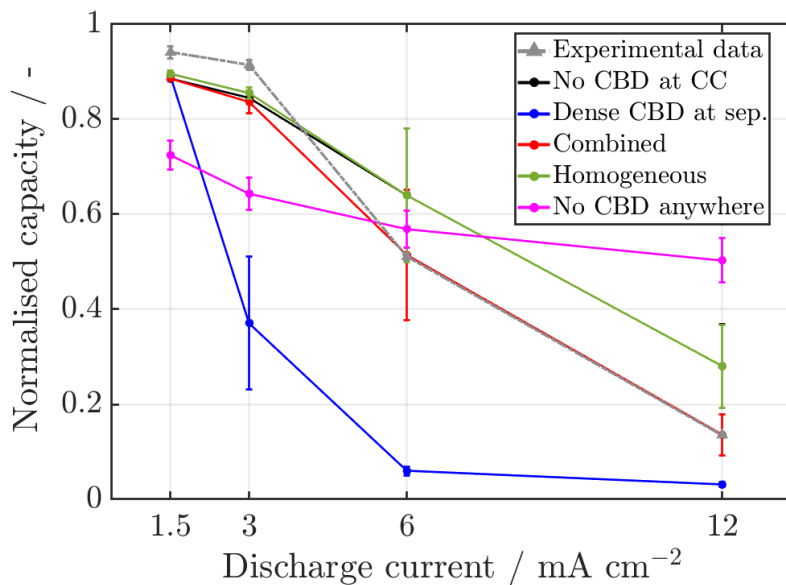


Figure 13: Summary of the discharge capacity for all scenarios introduced in Figure 2. Discharge capacity was determined at the lower cut-off voltage of 3.0 V after constant current discharge from 4.2 V. Capacities for both the experiments (gray color) and simulations (solid lines) were normalised to their theoretical capacity. The figure focuses on an electrode with density of 3.0 g/cm<sup>3</sup>.

634 The effect of different scenarios on concentration and flux distributions at  
 635 different currents is presented in the Supporting Information, providing ad-  
 636 ditional insights on limiting processes (see Section SI 4.2.2.).

#### 637 4.2.3. Effect of calendaring

638 In this section we will address the effect of electrode calendaring, with a  
 639 specific focus on the “Combined” case at all discharge current densities. Fig-  
 640 ure 14 shows the experimental and simulation results at increasing discharge  
 641 currents. The simulation results are given in colour and the experimental  
 642 data in gray-scale.

643 *Experimental results.* We can see from Figure 14 (a) that the lowest density  
 644 electrode, 2.7 g/cm<sup>3</sup>, provides the highest practical capacity at all currents.  
 645 This electrode has a 60% higher ionic conductivity than the 3.3 g/cm<sup>3</sup> elec-  
 646 trode and hence, a much lower pore transport impedance (see Supporting  
 647 Information Section SI 3.2.). Electrodes with 3.0 and 3.3 g/cm<sup>3</sup> densities  
 648 show similar performance in the rate tests. However, the highest density

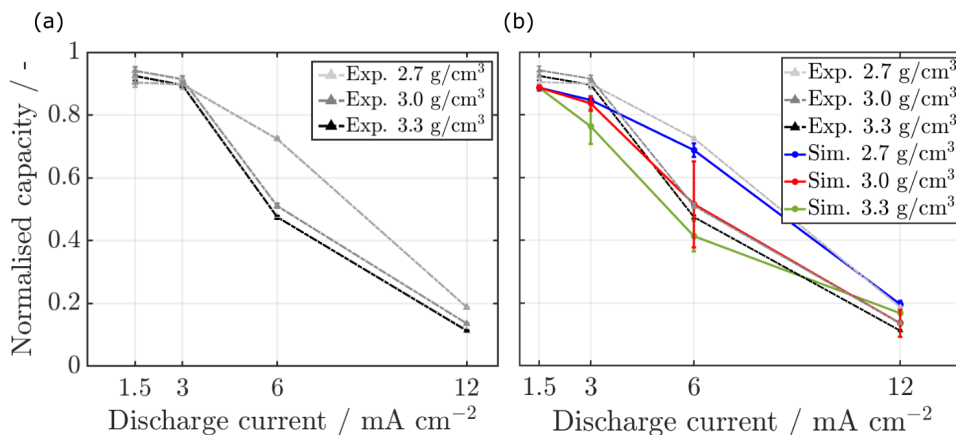


Figure 14: Plot (a) shows the end-of-discharge (at 3.0 V) capacity for measurements (in gray) at three different electrode densities for varying discharge currents. Plot (b) shows the average end-of-discharge (at 3.0 V) simulated capacity at all electrode densities for the “Combined” scenario at all discharge currents. The end capacities for the experiments and simulations were normalised to their theoretical capacity value. The standard deviation arises from considering all cutouts for each electrode. The abbreviations “Exp.” and “Sim.” stand for experimental data and simulation results, respectively.

649 electrode provides a slightly lower capacity at all currents. This trend is  
 650 in-line with our previous conclusion on the different scenarios: slow ionic  
 651 transport, in this case due to lower porosity, has a significantly more effect  
 652 on performance compared to reduced effective electronic conductivity.

653 *Simulation data.* Figure 14 (b) shows the corresponding simulation results.  
 654 Symbols indicate the average of the three electrode cutouts and the plot  
 655 additionally shows the standard deviation at each data point. Generally,  
 656 simulations are in-line with the experimental data (in gray). The electrodes  
 657 all match the trend seen in the experiments except at the lowest current  
 658 density. At 1.5 mA/cm<sup>2</sup>, eventhough the individual capacities of the electrodes  
 659 are comparable to the experiments, the shift between the electrode densi-  
 660 ties is not as obvious as in the experimental data. With increasing current  
 661 densities, the resulting capacities diverge and match the trend as seen in the  
 662 measurements.

663 Looking at each electrode density individually, we observe good agreement  
 664 between the experiments and simulations for the electrodes with a density  
 665 of 2.7 g/cm<sup>3</sup>. Interestingly, the standard deviations are smaller here, in  
 666 comparison to the wider spread seen in the corresponding impedance data.

667 Deviations in the impedance spectra can be allocated to electrical properties,  
668 which is less pronounced in the discharge simulations.

669 When considering the mid-density electrode, again, a good agreement to  
670 the experimental data is seen. However, we also observe larger deviations  
671 in practical capacities, which is arising from differences in the ionic con-  
672 duction pathways between the three cutouts. We have to emphasize, that  
673 in our study, we only adjust the thicknesses of the layers to the impedance  
674 data. Hence, the information is limited and does not allow to deduce the real  
675 configuration in the electrodes. Still, the qualitative agreement with the ex-  
676 perimental data indicates that we assign observed features in the impedance  
677 spectra to the relevant transport processes.

678 In order to visualise these processes, Figure 15 illustrates the distribution  
679 of the lithium-ion flux and cathode AM lithiation grade across the electrode  
680 for all the densities at 6 mA/cm<sup>2</sup> discharge current. The flux of the lithium  
681 ions in the electrolyte indicates the active volume of the electrode. With  
682 increasing electrode density, the region with high flux densities close to the  
683 separator decreases. At a density of 2.7 g/cm<sup>3</sup>, around two-thirds of the elec-  
684 trode shows high ionic flux density and a high lithiation of the cathode AM  
685 in the corresponding concentration distribution. Despite the high contact  
686 resistance, due to the low electronic conductivity close to the CC, there is  
687 moderate intercalation in this region. This confirms that thin layers without  
688 sufficient CBD network have a moderate effect on the capacity, yet a sig-  
689 nificant effect on the symmetric impedance. At increasing current densities  
690 (see Supporting Information Section 4.2.2.), only one-third of the 2.7 g/cm<sup>3</sup>  
691 electrode shows high flux of lithium ions. As a consequence, the utilisation  
692 of the cathode AM is significantly lower. Although the capacity drop at  
693 this current in the 3.3 g/cm<sup>3</sup> electrode is most drastic, visually, the length  
694 of lithiated AM as a fraction of the total electrode thickness is higher here  
695 than at the other densities (see Supporting Information Section 4.2.2.). This  
696 could be an advantageous side-effect of calendaring the electrodes, rendering  
697 the resistance to ion flux at the separator smaller. It is, therefore, critical  
698 to resolve the electrode microstructure for the simulations, and consider the  
699 effects of electrode processing steps on the local CBD properties.

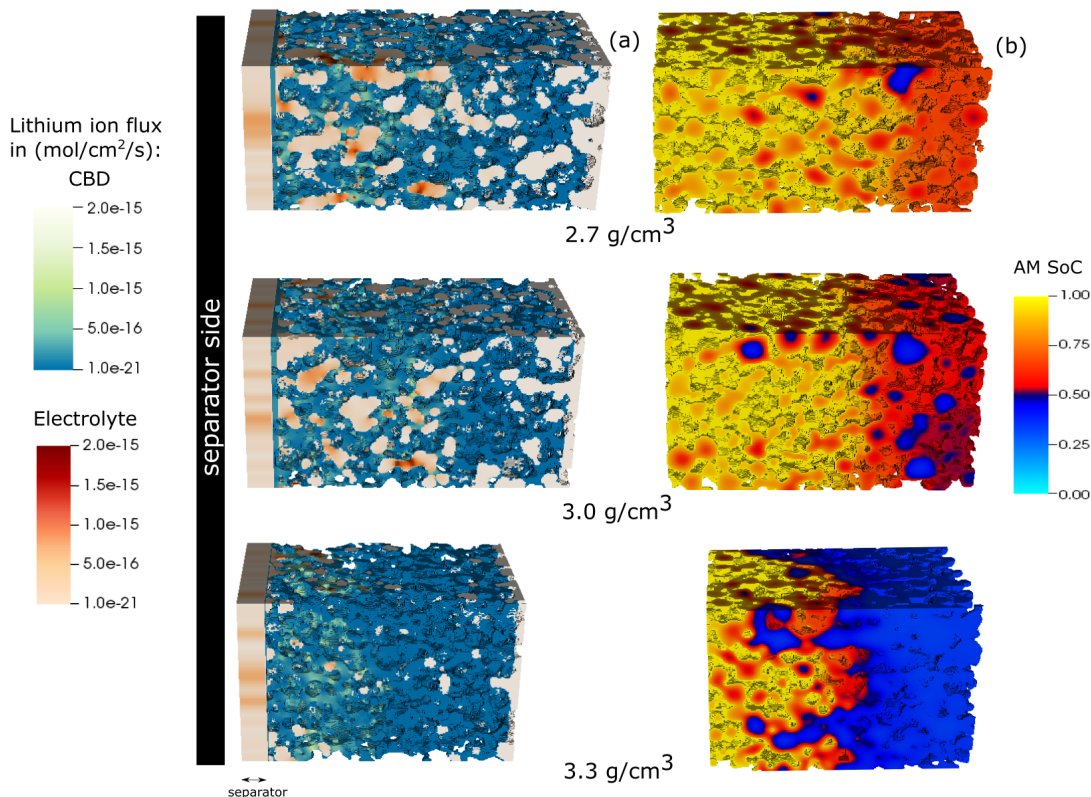


Figure 15: 3D material distribution in “Combined” case electrodes with densities of 2.7, 3.0 and 3.3 g/cm<sup>3</sup> at the lower cut-off (3.0 V) of a lithiation simulation with 6 mA/cm<sup>2</sup> constant current. (a) Flux of lithium-ion in the CBD (shown by the orange colour scale) and mesoporous space (blue colour scale). (b) Cathode AM state-of-charge (SoC) representing the normalized lithium distribution in an electrode with varying densities. The separator is on the left hand side of the 3D distribution in each panel and the current collector is to the right.

## 700 5. Summary and conclusions

701 In this paper, we investigate the effect of an inhomogeneous CBD distri-  
 702 bution on electrode impedance and rate performance. Such inhomogeneities  
 703 have been reported for high drying rates, especially in electrodes with high  
 704 areal density. An indicative feature for inhomogeneities in the electrode mi-  
 705 crostructure is an additional semi-circle which is observed at high frequencies  
 706 in the impedance spectra of symmetric cells under blocking conditions. Al-  
 707 though semicircular in shape, characteristic frequencies of this feature are

708 higher compared to those of charge transfer processes. In our study, we  
709 investigate different scenarios of an inhomogeneous binder distribution for  
710 different electrode densities. In particular, we found that both a dense layer  
711 of CBD close to the separator, and a CBD-free layer close to the CC are able  
712 to reproduce the semi-circle in the impedance. Considering the two cases  
713 provides the best match to the experimental data and is in-line with com-  
714 mon concepts of binder migration. In addition to the impedance spectra,  
715 we simulate lithiation of the electrodes in a half-cell configuration. These  
716 simulations clearly show that dense layers of CBD have a detrimental effect  
717 on discharge capacity. The scenario reproducing the symmetric impedance  
718 spectra with a dense layer of CBD close to the separator shows very poor  
719 discharge performance. On the other hand, scenario with only a CBD-absent  
720 layer close to the current collector overestimates the discharge capacity sig-  
721 nificantly. Again, the best match with the experimental data was found for  
722 an electrode bearing the two effects. Therefore, we can show that combining  
723 information from symmetric cell impedance spectra and half-cell rate tests  
724 provides significant insights on passive material distribution and thus, the  
725 rate limiting processes. Additionally, we could also shed light on the impor-  
726 tance of choosing process parameters preventing the migration of the CBD to  
727 the surface, since it is much more detrimental to performance from an elec-  
728 trochemical perspective, compared to CBD depleted layers at the current  
729 collector.

## 730 **6. Acknowledgements**

731 This work has been funded by the Bundesministerium für Bildung und  
732 Forschung within the project HiStructures under the reference Nos. 03XP0243A,  
733 03XP0243D and 03XP0243E. Particularly the work of Lea Kremer for prepar-  
734 ing the electrodes and contributing the related data, and Daniel Westhoff for  
735 segmenting the 3D image data obtained by synchrotron tomography. The  
736 authors also acknowledge the funding and support by the German Research  
737 Foundation (DFG) within the research training group SiMET under the  
738 project number 281041241/GRK2218. And last, but not least, the state of  
739 Baden-Württemberg through bwHPC and the German Research Foundation  
740 (DFG) through grant number INST 40/575-1 FUGG (JUSTUS 2 cluster).

741 **7. References**

- 742 [1] L. S. Kremer, A. Hoffmann, T. Danner, S. Hein, B. Prifling, D. Westhoff,  
743 C. Dreer, A. Latz, V. Schmidt, M. Wohlfahrt-Mehrens, Manufacturing  
744 process for improved ultra-thick cathodes in highenergy lithiumion bat-  
745 teries, *Energy Technology* 8 (2019) 1900167.
- 746 [2] D. Li, Q. Lv, C. Zhang, W. Zhou, H. Guo, S. Jiang, Z. Li, The effect  
747 of electrode thickness on the high-current discharge and long-term cycle  
748 performance of a lithium-ion battery, *Batteries* 8 (8) (2022) 101.
- 749 [3] M. Xu, B. Reichman, X. Wang, Modeling the effect of electrode thick-  
750 ness on the performance of lithium-ion batteries with experimental val-  
751 idation, *Energy* 186 (2019) 115864.
- 752 [4] H. Zheng, J. Li, X. Song, G. Liu, V. S. Battaglia, A comprehensive  
753 understanding of electrode thickness effects on the electrochemical per-  
754 formances of Li-ion battery cathodes, *Electrochimica Acta* 71 (2012)  
755 258–265.
- 756 [5] M. Indrikova, S. Grunwald, F. Golks, A. Netz, B. Westphal, A. Kwade,  
757 The morphology of battery electrodes with the focus of the conductive  
758 additives paths, *Journal of the Electrochemical Society* 162 (10) (2015)  
759 A2021–A2025.
- 760 [6] B. Lestriez, Functions of polymers in composite electrodes of lithium ion  
761 batteries, *Comptes Rendus Chimie* 13 (11) (2010) 1341–1350.
- 762 [7] J. Chen, J. Liu, Y. Qi, T. Sun, X. Li, Unveiling the roles of binder in  
763 the mechanical integrity of electrodes for lithium-ion batteries, *Journal*  
764 *of The Electrochemical Society* 160 (9) (2013) A1502–A1509.
- 765 [8] J. Entwistle, R. Ge, K. Pardikar, R. Smith, D. Cumming, Carbon binder  
766 domain networks and electrical conductivity in lithium-ion battery elec-  
767 trodes: A critical review, *Renewable and Sustainable Energy Reviews*  
768 166 (2022) 112624.
- 769 [9] M. Lain, E. Kendrick, Understanding the limitations of lithium ion bat-  
770 teries at high rates, *Journal of Power Sources* 493 (2021) 229690.

- 771 [10] F. Jiang, P. Peng, Elucidating the performance limitations of lithium-ion  
772 batteries due to species and charge transport through five characteristic  
773 parameters, *Scientific Reports* 6 (2016) 32639.
- 774 [11] L. Rao, X. Jiao, C.-Y. Yu, A. Schmidt, C. O’Meara, J. Seidt, J. R. Sayre,  
775 Y. M. Khalifa, J.-H. Kim, Multifunctional composite binder for thick  
776 high-voltage cathodes in lithium-ion batteries, *ACS Applied Materials*  
777 & *Interfaces* 14 (1) (2022) 861–872.
- 778 [12] A. Hoffmann, E. A. Heider, C. Dreer, C. Pfeifer, M. Wohlfahrt-Mehrens,  
779 Influence of the mixing and dispersing process on the slurry proper-  
780 ties and the microstructure and performance of ultrathick cathodes for  
781 lithium-ion batteries, *Energy Technology* 11 (5) (2023) 2200484.
- 782 [13] J. K. Mayer, L. Almar, E. Asylbekov, W. Haselrieder, A. Kwade, A. We-  
783 ber, H. Nirschl, Influence of the carbon black dispersing process on  
784 the microstructure and performance of Li-ion battery cathodes, *Energy*  
785 *Technology* 8 (2) (2020) 1900161.
- 786 [14] J. K. Mayer, H. Bockholt, A. Kwade, Inner carbon black porosity as  
787 characteristic parameter for the microstructure of lithium-ion electrodes  
788 and its effect on physical and electrochemical properties, *Journal of*  
789 *Power Sources* 529 (2022) 231259.
- 790 [15] G. Liu, H. Zheng, S. Kim, Y. Deng, A. M. Minor, X. Song, V. S.  
791 Battaglia, Effects of various conductive additive and polymeric binder  
792 contents on the performance of a lithium-ion composite cathode, *Journal*  
793 *of The Electrochemical Society* 155 (2008) A887.
- 794 [16] M. Nikpour, B. Liu, P. Minson, Z. Hillman, B. A. Mazzeo, D. R.  
795 Wheeler, Li-ion electrode microstructure evolution during drying and  
796 calendaring, *Batteries* 8 (2022) 107.
- 797 [17] S. Jaiser, M. Müller, M. Baunach, W. Bauer, P. Scharfer, W. Schabel,  
798 Investigation of film solidification and binder migration during drying  
799 of Li-ion battery anodes, *Journal of Power Sources* 318 (2016) 210–219.
- 800 [18] Y. Su, K. Zhou, Y. Yuan, W. Liu, Y. Deng, Study on prediction of binder  
801 distribution in the drying process of the coated web of positive electrode  
802 for lithium ion battery, *IOP Conference Series: Materials Science and*  
803 *Engineering* 793 (1) (2020) 012025.

- 804 [19] J. Landesfeind, A. Eldiven, H. A. Gasteiger, Influence of the binder on  
805 lithium ion battery electrode tortuosity and performance, *Journal of the*  
806 *Electrochemical Society* 165 (5) (2018) A1122–A1128.
- 807 [20] H. Wiese, K. Weil, An efficient Fourier transform algorithm for frequency  
808 domains of several decades using logarithmically spaced time samples,  
809 *IEEE Transactions on Acoustics, Speech, and Signal Processing* 36 (7)  
810 (1988) 1096–1099.
- 811 [21] M. Doyle, J. P. Meyers, J. Newman, Computer simulations of the  
812 impedance response of lithium rechargeable batteries, *Journal of The*  
813 *Electrochemical Society* 147 (1) (2000) 99.
- 814 [22] C. Chen, J. Liu, K. Amine, Symmetric cell approach and impedance  
815 spectroscopy of high power lithium-ion batteries, *Journal of Power*  
816 *Sources* 96 (2) (2001) 321–328.
- 817 [23] N. Ogihara, S. Kawauchi, C. Okuda, Y. Itou, Y. Takeuchi, Y. Ukyo, The-  
818oretical and experimental analysis of porous electrodes for lithium-ion  
819batteries by electrochemical impedance spectroscopy using a symmet-  
820ric cell, *Journal of The Electrochemical Society* 159 (7) (2012) A1034–  
821A1039.
- 822 [24] D. W. Dees, D. P. Abraham, W. Lu, K. G. Gallagher, M. Bettge, A. N.  
823Jansen, Electrochemical modeling and performance of a lithium- and  
824manganese-rich layered transition-metal oxide positive electrode, *Jour-  
825nal of The Electrochemical Society* 162 (4) (2015) A559–A572.
- 826 [25] M. Schönleber, C. Uhlmann, P. Braun, A. Weber, E. Ivers-Tiffée, A  
827consistent derivation of the impedance of a lithium-ion battery elec-  
828trode and its dependency on the state-of-charge, *Electrochimica Acta*  
829243 (2017) 250–259.
- 830 [26] S. Gantenbein, M. Weiss, E. Ivers-Tiffée, Impedance based time-domain  
831modeling of lithium-ion batteries: Part I, *Journal of Power Sources* 379  
832(2018) 317–327.
- 833 [27] R. Morasch, J. Landesfeind, B. Suthar, H. A. Gasteiger, Detection of  
834binder gradients using impedance spectroscopy and their influence on  
835the tortuosity of Li-ion battery graphite electrodes, *Journal of the Elec-  
836trochemical Society* 165 (14) (2018) A3459–A3467.

- 837 [28] T.-T. Nguyen, The study of the correlation between the microstruc-  
838 tural properties and the electrochemical performance of the Li-ion bat-  
839 tery high-energy-density positive electrode, Doctoral thesis, Université  
840 de Picardie Jules Verne (2021).
- 841 [29] J. Landesfeind, M. Ebner, A. Eldiven, V. Wood, H. A. Gasteiger, Tortu-  
842 osity of battery electrodes: Validation of impedance-derived values and  
843 critical comparison with 3D tomography, *Journal of The Electrochemi-  
844 cal Society* 165 (3) (2018) A469–A476.
- 845 [30] J. E. Vogel, M. M. Forouzan, E. E. Hardy, S. T. Crawford, D. R.  
846 Wheeler, B. A. Mazzeo, Electrode microstructure controls localized elec-  
847 tronic impedance in Li-ion batteries, *Electrochimica Acta* 297 (2019)  
848 820–825.
- 849 [31] S. Hein, T. Danner, D. Westhoff, B. Prifling, R. Scurtu, L. Kremer,  
850 A. Hoffmann, A. Hilger, M. Osenberg, I. Manke, M. Wohlfahrt-Mehrens,  
851 V. Schmidt, A. Latz, Influence of conductive additives and binder on  
852 the impedance of lithium-ion battery electrodes: Effect of morphology,  
853 *Journal of The Electrochemical Society* 167 (2020) 013546.
- 854 [32] J. Landesfeind, J. Hattendorff, A. Ehrl, W. A. Wall, H. A. Gasteiger,  
855 Tortuosity determination of battery electrodes and separators by  
856 impedance spectroscopy, *Journal of The Electrochemical Society* 163 (7)  
857 (2016) A1373–A1387.
- 858 [33] A. Shodiev, E. N. Primo, M. Chouchane, T. Lombardo, A. C. Ngand-  
859 jong, A. Rucci, A. A. Franco, 4D-resolved physical model for electro-  
860 chemical impedance spectroscopy of  $\text{Li}(\text{Ni}_{1-x-y}\text{Mn}_x\text{Co}_y)\text{O}_2$ -based cath-  
861 odes in symmetric cells: Consequences in tortuosity calculations, *Jour-  
862 nal of Power Sources* 454 (2020) 227871.
- 863 [34] M. Gaberscek, J. Moskon, B. Erjavec, R. Dominko, J. Jamnik, The  
864 importance of interphase contacts in Li ion electrodes: The meaning  
865 of the high-frequency impedance arc, *Electrochemical and Solid-State  
866 Letters* 11 (10) (2008) A170.
- 867 [35] R. Kant, M. B. Singh, Theory of the electrochemical impedance of  
868 mesostructured electrodes embedded with heterogeneous micropores,  
869 *The Journal of Physical Chemistry C* 121 (13) (2017) 7164–7174.

- 870 [36] K. Miyasaka, K. Watanabe, E. Jojima, H. Aida, M. Sumita, K. Ishikawa,  
871 Electrical conductivity of carbon-polymer composites as a function of  
872 carbon content, *Journal of Materials Science* 17 (1) (1982) 1610–1616.
- 873 [37] B. L. Trembacki, A. N. Mistry, D. R. Noble, M. E. Ferraro, P. P. Mukher-  
874 jee, S. A. Roberts, Mesoscale analysis of conductive binder domain mor-  
875 phology in lithium-ion battery electrodes, *Journal of the Electrochemical*  
876 *Society* 165 (13) (2018) E725–E736.
- 877 [38] R. Dominko, M. Gaberscek, J. Drofenik, M. Bele, S. Pejovnik, J. Jamnik,  
878 The role of carbon black distribution in cathodes for Li ion batteries,  
879 *Journal of Power Sources* 119-121 (2003) 770–773.
- 880 [39] S. Liu, X. Zeng, D. Liu, S. Wang, L. Zhang, R. Zhao, F. Kang, B. Li,  
881 Understanding the conductive carbon additive on electrode/electrolyte  
882 interface formation in lithium-ion batteries via in situ scanning electro-  
883 chemical microscopy, *Frontiers in Chemistry* 8 (2020) 114.
- 884 [40] Y. K. Lee, The effect of active material, conductive additives, and binder  
885 in a cathode composite electrode on battery performance, *Energies* 12  
886 (4) (2019) 658.
- 887 [41] F. Jeschull, J. Maibach, K. Edström, D. Brandell, On the electrochemi-  
888 cal properties and interphase composition of graphite: PVdF-HFP elec-  
889 trodes in dependence of binder content, *Journal of The Electrochemical*  
890 *Society* 164 (7) (2017) A1765.
- 891 [42] G. Liu, H. Zheng, S. Kim, Y. Deng, A. M. Minor, X. Song, V. S.  
892 Battaglia, Effects of various conductive additive and polymeric binder  
893 contents on the performance of a lithium-ion composite cathode, *Journal*  
894 *of The Electrochemical Society* 155 (12) (2008) A887.
- 895 [43] T. Knorr, S. Hein, B. Prifling, M. Neumann, T. Danner, V. Schmidt,  
896 A. Latz, Simulation-based and data-driven techniques for quantifying  
897 the influence of the carbon binder domain on electrochemical properties  
898 of Li-ion batteries, *Energies* 15 (2022) 7821.
- 899 [44] A. Mistry, S. Trask, A. Dunlop, G. Jeka, B. Polzin, P. P. Mukherjee,  
900 V. Srinivasan, Quantifying negative effects of carbon-binder networks  
901 from electrochemical performance of porous Li-ion electrodes, *Journal*  
902 *of The Electrochemical Society* 168 (7) (2021) 070536.

- 903 [45] B. Priffling, M. Neumann, S. Hein, T. Danner, E. Heider, A. Hoffmann,  
904 P. Rieder, A. Hilger, M. Osenberg, I. Manke, M. Wohlfahrt-Mehrens,  
905 A. Latz, V. Schmidt, Quantitative comparison of different approaches for  
906 reconstructing the carbon-binder domain from tomographic image data  
907 of cathodes in lithium-ion batteries and its influence on electrochemical  
908 properties, *Energy Technology* 11 (2022) 2200784.
- 909 [46] F. Boso, W. Li, K. Um, D. M. Tartakovsky, Impact of carbon binder  
910 domain on the performance of lithium-metal batteries, *Journal of The  
911 Electrochemical Society* 169 (10) (2022) 100550.
- 912 [47] A. Chauhan, E. Asylbekov, S. Kesper, H. Nirschl, Influence of carbon  
913 binder domain on the performance of lithium-ion batteries: Impact  
914 of size and fractal dimension, *Electrochemical Science Advances* 3 (1)  
915 (2023) e2100151.
- 916 [48] L. Zielke, T. Hutzenlaub, D. R. Wheeler, I. Manke, T. Arlt, N. Paust,  
917 R. Zengerle, S. Thiele, A combination of X-Ray tomography and car-  
918 bon binder modeling: Reconstructing the three phases of  $\text{LiCoO}_2$  Li-ion  
919 battery cathodes, *Advanced Energy Materials* 4 (8) (2014) 2–7.
- 920 [49] A. Li, J. L. Hempel, M. P. Balogh, Y.-T. Cheng, A. I. Taub, Effect of  
921 binder content on silicon microparticle anodes for lithium-ion batteries,  
922 *Journal of The Electrochemical Society* 170 (1) (2023) 010533.
- 923 [50] A. Latz, J. Zausch, Thermodynamic consistent transport theory of Li-  
924 ion batteries, *Journal of Power Sources* 196 (6) (2011) 3296–3302.
- 925 [51] A. Latz, J. Zausch, Multiscale modeling of lithium ion batteries: thermal  
926 aspects, *Beilstein Journal of Nanotechnology* 6 (2015) 987–1007.
- 927 [52] A. H. Wiedemann, G. M. Goldin, S. A. Barnett, H. Zhu, R. J. Kee,  
928 Effects of three-dimensional cathode microstructure on the performance  
929 of lithium-ion battery cathodes, *Electrochimica Acta* 88 (2013) 580–588.
- 930 [53] J. Feinauer, T. Brereton, A. Spetl, M. Weber, I. Manke, V. Schmidt,  
931 Stochastic 3D modeling of the microstructure of lithium-ion battery an-  
932 odes via Gaussian random fields on the sphere, *Computational Materials  
933 Science* 109 (2015) 137–146.

- 934 [54] W. Görner, M. P. Hentschel, B. R. Müller, H. Riesemeier, M. Krumrey,  
935 G. Ulm, W. Diete, U. Klein, R. Frahm, BAMline: The first hard X-ray  
936 beamline at BESSY II, Nuclear Instruments and Methods in Physics  
937 Research, Section A: Accelerators, Spectrometers, Detectors and Asso-  
938 ciated Equipment 467-468 (2001) 703–706.
- 939 [55] Fraunhofer Institute for Industrial Mathematics (ITWM), BEST - Bat-  
940 tery and Electrochemistry Simulation Tool (2020).  
941 URL <http://itwm.fraunhofer.de/best>
- 942 [56] A. Nyman, M. Behm, G. Lindbergh, Electrochemical characterisation  
943 and modelling of the mass transport phenomena in LiPF<sub>6</sub>-EC-EMC elec-  
944 trolyte, *Electrochimica Acta* 53 (22) (2008) 6356–6365.
- 945 [57] S. G. Meibuhr, Electrode studies in nonaqueous electrolytes, *Journal of*  
946 *The Electrochemical Society* 117 (1) (1970) 56.
- 947 [58] R. Amin, Y.-M. Chiang, Characterization of electronic and  
948 ionic transport in Li<sub>1-x</sub>Ni<sub>0.33</sub>Mn<sub>0.33</sub>Co<sub>0.33</sub>O<sub>2</sub> (NMC333) and  
949 Li<sub>1-x</sub>Ni<sub>0.50</sub>Mn<sub>0.20</sub>Co<sub>0.30</sub>O<sub>2</sub> (NMC523) as a function of Li content,  
950 *Journal of The Electrochemical Society* 163 (8) (2016) A1512–A1517.
- 951 [59] T. Danner, M. Singh, S. Hein, J. Kaiser, H. Hahn, A. Latz, Thick elec-  
952 trodes for Li-ion batteries: A model based analysis, *Journal of Power*  
953 *Sources* 334 (2016) 191–201.
- 954 [60] W. G. Bessler, Rapid impedance modeling via potential step and current  
955 relaxation simulations, *Journal of The Electrochemical Society* 154 (11)  
956 (2007) B1186–B1191.
- 957 [61] J. Ohser, F. Mücklich, *Statistical analysis of microstructures in materials*  
958 *science*, John Wiley & Sons, Chichester (2000).